Wolter Mirror Microscope: Novel Neutron Focussing and Imaging Optic

by

Yelena S. Bagdasarova

Submitted to the Department of Physics
in partial fulfillment of the requirements for the degree of

Bachelor of Science Physics

at the

MASSACHUSETTS INSTITUTE OF TECHNOLOGY

June 2010

Author .....
Department of Physics
May 18, 2010

Certified by .....
David E. Moncton
Professor
Thesis Supervisor

Certified by .....
Boris Khaykovich
Research Scientist
Thesis Supervisor

Accepted by .....
David Prichard
Cecial and Ida Green Professor of Physics

Wolter Mirror Microscope: Novel Neutron Focussing and Imaging Optic

by

Yelena S. Bagdasarova

Submitted to the Department of Physics
on May 18, 2010, in partial fulfillment of the
requirements for the degree of
Bachelor of Science Physics

Abstract

In this thesis, I investigated the effectiveness of a Wolter Type I neutron microscope as a focusing and imaging device for thermal and cold neutrons sources by simulating the performance of the optics in a standard neutron ray-tracing package. I used the simulation to optimize the Wolter mirror geometry for a particular case, deducing the primary constraints of the system on the delivery of maximal flux density to the focal spot and the advantages of nesting the mirrors. I explore the imaging aspects of the optics by simulating surface imperfections, such as figure errors and finish errors, and compare the resulting distortions in the focal spot to the no error case. I finally discuss the experimentation of real Wolter mirrors at the MIT Nuclear Reactor Laboratory and compare the tests to simulation predictions.

Thesis Supervisor: David E. Moncton
Title: Professor

Thesis Supervisor: Boris Khaykovich
Title: Research Scientist

Acknowledgments

I would like to thank Professor Moncton for giving me the opportunity to engage in a project of such depth and scope. I can certainly say that working on this project has caused me to grow tremendously as a scientist and independent researcher, and I am grateful to Professor Moncton for allowing me to work in an atmosphere that fostered such growth. I would primarily like to thank Boris Khaykovich for working so closely on this project with me and dedicating countless hours to patiently helping me understand and achieve the goals I set out to accomplish. I would like to thank him for pushing me to think independently and critically before looking to other resources for answers and for letting me take initiative for my own work. In addition, I would like to thank Mikhail Gubarev for volunteering his expertise in x-ray optics and his knowledge PSD functions for my use during this project. Finally, I would like to thank the MIT Physic Department for equipping me with the knowledge, skills, and confidence it takes to be an investigator of the physical world.

Contents

List of Figures

Chapter 1

Introduction

Neutron scattering methods are among the most important tools for studying the structure and dynamics of matter. The unique properties of neutrons as deeply penetrating, spin-interacting, and neutral make them choice particles for the probing of bulk materials, magnetic thin films, and nuclear structures. They are the preferred over x-rays and electrons in biological microscopy as they interact well with nitrogen and hydrogen while imparting comparatively less damage to the sample itself. In any microscopy or reflectometry experiment, a well-defined beam is essential. However, the assortment of instruments used to define neutron beams is still small in comparison to x-rays, mostly because neutrons are weakly interacting, making neutron beams are difficult to manipulate.

The purpose of this work will be to investigate and demonstrate the effectiveness of a novel neutron optics that might make neutron microscopy practical. This optics is based on an existing x-ray optics design known as Wolter optics. Its design consists of two Nickel-coated con-focal mirrors (elliptical or parabolic mirror followed by a hyperbolic mirror) that reflect neutron beams at grazing incidence from one focus to the other. The advantage of Wolter optics is that its geometry satisfies the Abbe sine condition almost exactly, the geometric condition that eliminates coma, resulting in near-perfect imaging of small, off-axis objects. In addition, every neutron is reflected only once by each mirror, limiting the effects of surface roughness and reflectivity on image quality and intensity.

The aim of this analysis is to explore the effectiveness of Wolter Type I neutron microscope as both a focusing and imaging device for cold and thermal neutron sources. To do this a simulation of the mirror design was written in McStas, a standard neutron ray-tracing software package. The module was used to conduct numerical experiments in order to illuminate the basic trends of the optics as a function of the geometry and properties of the mirror and source. Tests concentrated on optimizing the mirror for a few cases of focusing and imaging applications and measuring its performance by ways of flux-density and image quality at the focal spot. Variations on the basic mirror design, such as nesting the mirrors, were explored and evaluated, comparing to cases where no optics were present. Finally, the simulation was used to model a set of real mirrors that were tested at the MIT Nuclear Reactor Laboratory.

Chapter two defines the complete geometry of the Wolter-Type I microscope, the reflective properties of mirrors, and the simulation of the optics in McStas. Chapter three describes how the optics was optimized in order to achieve maximum flux at the focal spot, discussing the advantages of supermirrors and nesting. Chapter four focuses on the imaging aspects of the optics, particularly sources of surface error that distort image quality. Finally, Chapter five describes the testing of a real set of mirrors at the MIT Nuclear Reactor Laboratory.

Chapter 2

Wolter Optics: Geometry and Design

2.1 Specular Reflection

Alongside refraction and diffraction, reflection is one of three common optical methods for manipulating a beam while maintaining coherence. In the case of reflecting light, an incoming electromagnetic wave causes electrons in an atom to oscillate, which then produce dipole radiation. In this case, total reflection at a surface occurs when the the incident waves and the outgoing waves from each scatterer interfere in a way that leaves an identical wave-front, propagating back into the medium it came from at a new direction. We can explain reflection for neutrons in a similar way by treating neutrons as matter-waves.

We know from quantum mechanics that all can be treated as waves with wavelength λ relating to their momentum p by the de Broglie relation:

$$p = \frac{h}{\lambda} \tag{2.1}$$

where h is plank's constant. The relation between wavelength and energy is subsequently

$$E = \frac{\hbar^2 k^2}{2m} \tag{2.2}$$

where m is the particle mass and $k = \frac{2\pi}{\lambda}$ is defined as the magnitude of the wave vector. As in the case of electromagnetic waves, reflection for neutron waves is an interference phenomenon. The difference is that because of the neutrality of neutrons, the scatterer is the point-like nucleus instead of the electron cloud. Like with dipole radiation, the sum of all incident and scattered waves appears to be a reflection of the original wave-front off the surface. For ideally smooth surfaces, reflection will be specular, with the angle of incidence θ_i equalling the angle of scattering θ_s measured from the surface plane (Fig. 2.1). Total reflection (no transmission) for neutrons occurs when the the angle of incidence θ_i is less than the critical angle

$$\theta_c = \sqrt{\frac{\rho b}{\pi}}\lambda \tag{2.3}$$

where the ρ is the atomic density of the material and b is the scattering length which characterizes the strength of the nuclear interaction [4]. It is clear from (2.3) that surfaces with high values of ρb are desired to maximize θ_c for any given energy. Nickel has one of the highest values ($\rho b = 9.41 \times 10^{11}$ m^{-2}) and is consequently the most common material used to coat reflecting surfaces. For thermal to cold neutrons ($\lambda = 1 - 8$ Å) corresponding to respective energies of 811 meV, the critical angles ranges from $1.73 - 13.4$ mrad. Thus, neutrons of these typical energies, like x-rays, will reflect only at grazing incidence, necessitating the development of grazing-incidence optics in the arena of beamline instrumentation.

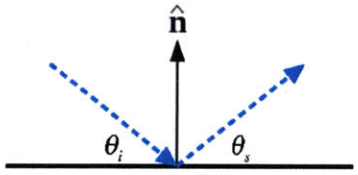

Figure 2-1: Specular reflection off an ideally smooth surface, where $\theta_i = \theta_s$.

2.2 Mirror Geometry

In 1952, Hans Wolter introduced three geometries for glancing x-ray telescopes, each involving a two-mirror system of confocal conic sections. The three types of telescopes are illustrated in Fig. 2.2. All three geometries are alike in that they utilize exactly two reflections to focus an incoming x-ray beam into a focus of one conic section.

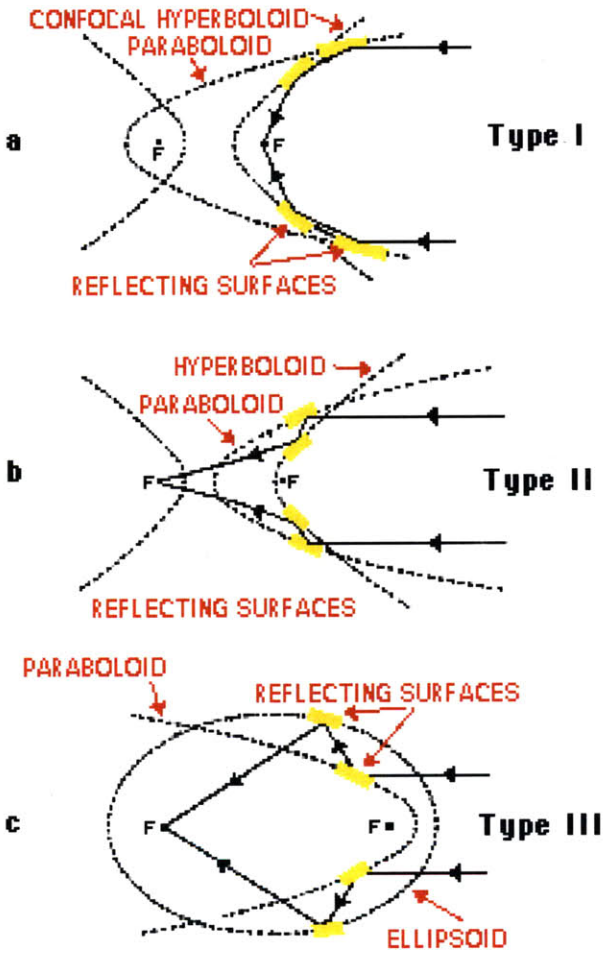

Figure 2-2: Type I, II and III Wolter Telescopes.

All three are also telescopes in that they focus highly collimated beams. Since typical neutron sources from reactors produce divergent beams, they call for a microscope analogue of the Wolter telescope. For the geometry of the Wolter Type I telescope, this coincides with replacing the paraboloid with an ellipsoid. The schematic in Fig. 2.3 defines the Wolter Type I microscope geometry in terms of the length of the system

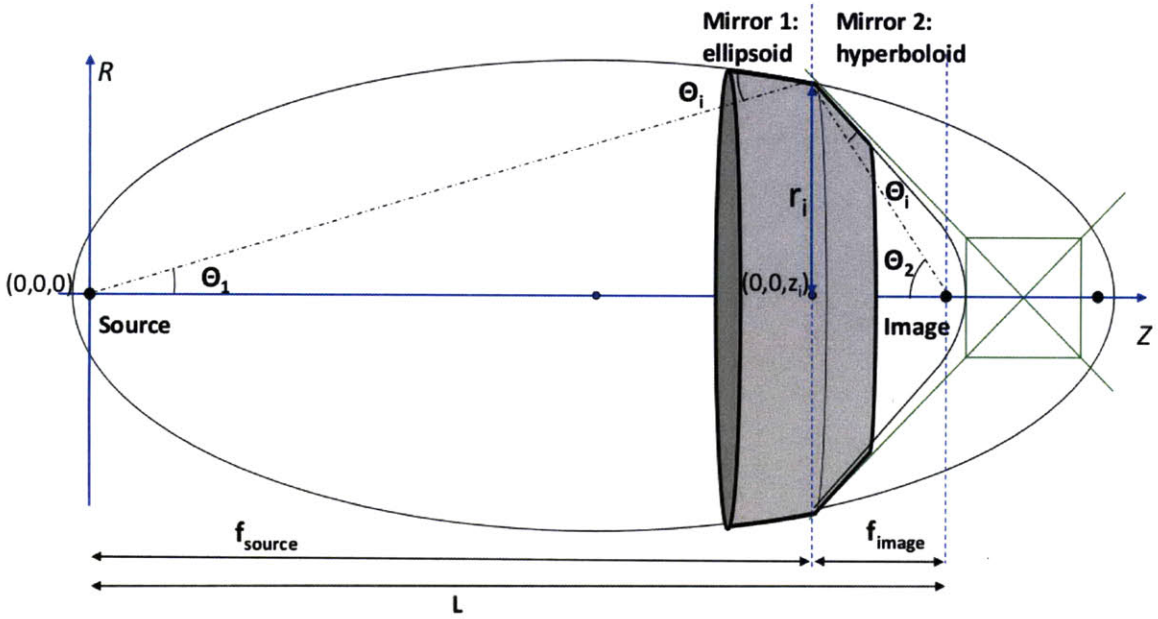

Figure 2-3: Schematic drawing of Wolter Type I microscope consisting of confocal ellipsoid and hyperboloid mirrors. The source is located at the left focus of the ellipsoid, corresponding to the origin of the coordinate system. The image is formed at the left focus of the hyperboloid at $(0, 0, L)$ where L is the length from the source to the image. The right focus of the ellipsoid is coincident with the right focus of the hyperboloid (the right sheet is not shown). r_i is the radius of the two mirrors at their point of intersection, z_i is the axial distance to the intersection from the origin, and Θ_i is the grazing angle on either side of the intersection point and is forced to be the same for both mirrors. f_{source} and f_{image} are the focal distances from each focus to the intersection while Θ_1 and Θ_2 are the angles subtending the intersection point from each focus.

L, the radius of the mirrors at the point of intersection r_i, and the magnification of the system M. The magnification of the ellipsoid-hyperboloid system in Fig. 2.3 is defined as the ratio of focal lengths

$$M = \frac{\Theta_1}{\Theta_2} = \frac{f_{image}}{f_{source}} \tag{2.4}$$

and is also the ratio of image to source size. Only rays that reflect off the ellipsoid will reflect off the hyperboloid and into the focal spot. Neutrons that are not doubly reflected are not focused. The last condition in place is for the grazing angle at the intersection Θ_i to be the same for both mirrors, making the intersection of the two

mirrors smooth. The equation for this condition is

$$\Theta_i = \frac{1}{4}(\Theta_1 + \Theta_2) \tag{2.5}$$

and arises from the geometrric properties of the ellipse and the hyperbola. The standard equations governing the ellipsoid and hyperboloid are

$$F(z,r) = b^2(z - z_0)^2 + a^2r^2 - a^2b^2 = 0 \tag{2.6}$$
$$a^2 - b^2 = c^2$$

and

$$F(z,r) = b^2(z - z_0)^2 - a^2r^2 - a^2b^2 = 0 \tag{2.7}$$
$$a^2 + b^2 = c^2$$

where a, b, and z_0 in each equation is the semi-major axis, semi-minor axis, and the position of the center along the optical axis (z-axis) respectively. Using geometry, we can solve for c and z_0 for both conic sections and find for the ellipsoid

$$c = \frac{1}{2}\left[\frac{r_i}{\tan(\Theta_2 - 2\Theta_i)} + z_i\right] \tag{2.8}$$
$$z_0 = c$$

and for the hyperboloid

$$c = \frac{1}{2}\left[\frac{r_i}{\tan(\Theta_2 - 2\Theta_i)} - z_i\right] \tag{2.9}$$
$$z_0 = L + c$$

We can subsequently solve the equations in (2.6) and (2.7) for a and b by evaluating both equations at the intersection (z_i, r_i). Finally, two additional parameters that define the system are the physical lengths of the mirrors which partly determine the

effective cross-section of the mirrors, or the area of the total beam that they collect.

2.3 Geometric Advantages for Imaging

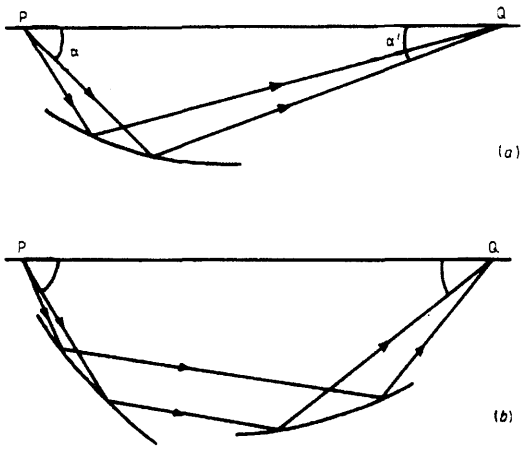

Figure 2-4: In the case of a single reflection (a) the Abbe sine condition cannot be satisfied. It may be satisfied if an even number of reflections occurs (b). [3]

For any optic, aberration, or the failure of rays to converge at the focal spot, degrades image quality. Two common types of aberrations are spherical aberrations, affecting off-axis points in the source, and astigmatism, where rays reflecting through different planes are focussed at different points along the optical axis. Because Wolter mirrors are aspheric and axially symmetric, images from extended sources are free from spherical aberrations and suffer only from third-order astigmatism. In addition, the Wolter Type I microscope nearly exactly satisfies the Abbe sine condition

$$\frac{\sin\alpha}{\sin\alpha'} \tag{2.10}$$

where α and α' are the angles between the rays and the optical axis shown in Fig. 2.4. If the condition is satisfied exactly, the magnification is constant over the entire mirror and the focal spot is a perfectly scaled image of the source (it is a coma-free optic). It can be shown that this condition is nearly satisfied for the Wolter Type I microscope provided that the diameter of the mirrors (and consequently Θ_1 and Θ_2)

are small [3]. The result is a near-perfect imaging optic, where image distortion is due to surface imperfections rather than the geometry of the optics.

2.4 Ray-Tracing

Using the parameters and equations above, we are able to simulate the focusing properties of the Wolter Type I microscope by tracing the path that each neutron of a given velocity takes through the optics. Given an incoming velocity $\vec{v_i}$, the velocity $\vec{v_s}$ of the specularly reflected neutron can be computed from the surface normal $\hat{n}$ by

$$\vec{v_s} = \vec{v_i} - 2(\vec{v} \cdot \hat{n})\hat{n} \tag{2.11}$$

where $\hat{n}$ for the hyperboloid surface $F(z, r)$ in (2.7) is

$$\vec{n} = \nabla F(z, r) = \begin{pmatrix} -a^2 x \\ -a^2 y \\ b^2(z - z_0) \end{pmatrix} \tag{2.12}$$

Every change to the path of the neutron can thus be modeled by a specular reflection from either the ellipsoid and hyperboloid if all defining parameters are known. Whether a nuetron is actually reflected or absorbed by the surface is determined by a reflectivity curve $R(\theta_i)$ particular to the surface and the wavelength of the nuetron. Usually $R(\theta_i)$ is the Fresnel reflectivity curve. In the simplest approximation, $R(\theta_i)$ is the step function

$$R(\theta_i) = \begin{cases} 1 & \text{if } \theta_i < \theta_c \\ 0 & \text{if } \theta_i > \theta_c, \end{cases} \tag{2.13}$$

Chapter 3

Optimizing for Maximum Flux Density

Most often, the purpose of non-imaging focusing optics is to irradiate a sample with as much flux as possible. Depending on the application of beam, constraints such as spot size, the length of the system, and source properties, also factor into the optimization process. To assess the collecting power of the Wolter Type I microscope, the optic was simulated in the ray-tracing software package McStas and optimized for different system lengths and magnifications. Basic geometric factors, such as the effective cross section of the mirror, as well as mirror reflectivity were observed as the primary constraints on delivered flux to the focus. Beyond standard geometric optimization, nesting and supermirrors were found to be two effective techniques to enhance collection. Finally, for thoroughness, the effectiveness of the Wolter system was demonstrated by a simple comparison to the case where no optics is present.

3.1 Supermirrors

One straightforward approach to maximizing the focusing power of an optic is to maximize its reflectivity. This can be achieved by increasing the critical angle of the reflecting surface and is done by way of multilayers in supermirrors. Common neutron supermirrors consist of hundreds to thousands of alternating Nickel-Titanium layers

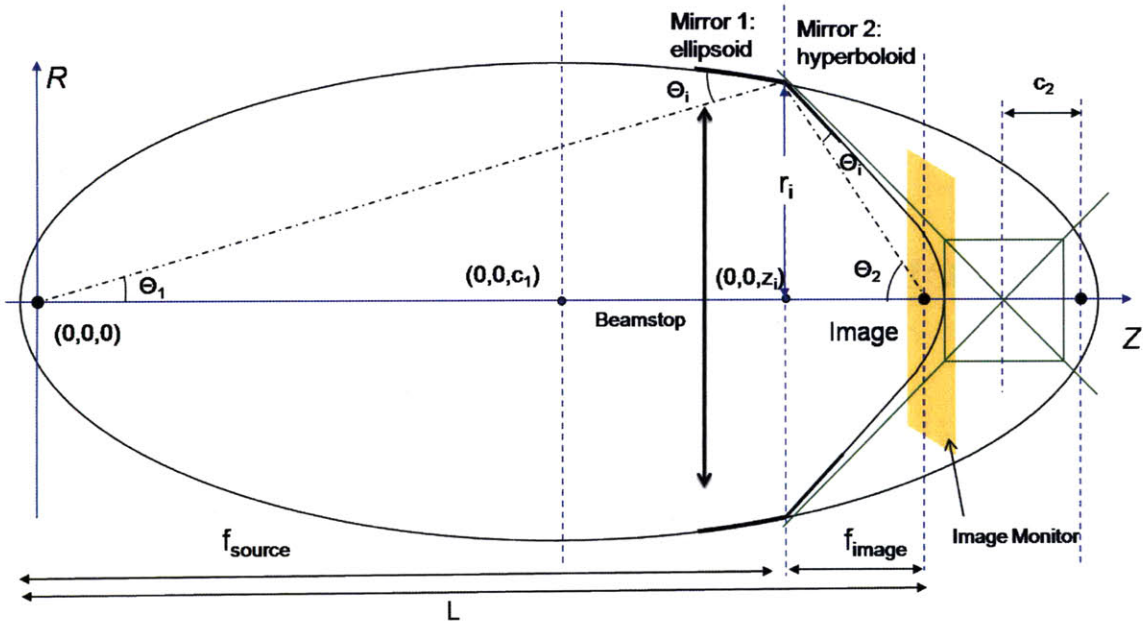

Figure 3-1: Schematic drawing of Wolter Type I microscope consisting of confocal ellipsoid and hyperboloid mirrors. Mirror geometry defined by system length L, magnification M, and mirror radius at intersection r_i. Remaining parameters defined in Fig. 1 of Chapter 2.

and have larger critical angles than single-layer Nickel mirrors due to interference effects [2]. The relation between the critical angles θ_m and θ_c in supermirrors and single-layer Ni mirrors respectively is

$$\theta_m = m\theta_c \tag{3.1}$$

where the factor m depends on the number of layers in the supermirror. Typical values of m are 2 for 100 layers and 3 for 500 layers.

3.2 Optimizing Geometry

In several simulated tests, Wolter Type I $m = 3$ supermirrors were optimized to yield the maximum flux density at the focal spot. Fig. 3.1 is a schematic of the optimized Wolter mirror geometry defined in Chapter two, where the parameters of the system are the distance between the foci L, radius r_i, magnification M, and the length of the

mirror segments l_{mirror}. Generally, the lengths of the mirror segments will scale with r_i by virtue of manufacturing constraints. In this simulation, we chose $l_{mirror} = 10r_i$ and capped the length of the segments at 700 mm. The source used in this simulation was circular, uniformly divergent, and monochromatic ($r = 5$ mm, divergence $= 1$ deg, $E = 5$ meV). A beamstop was placed at the entrance of the ellipsoid to remove neutrons whose trajectories did not intersect with the first mirror and therefore would not contribute to the focal spot.

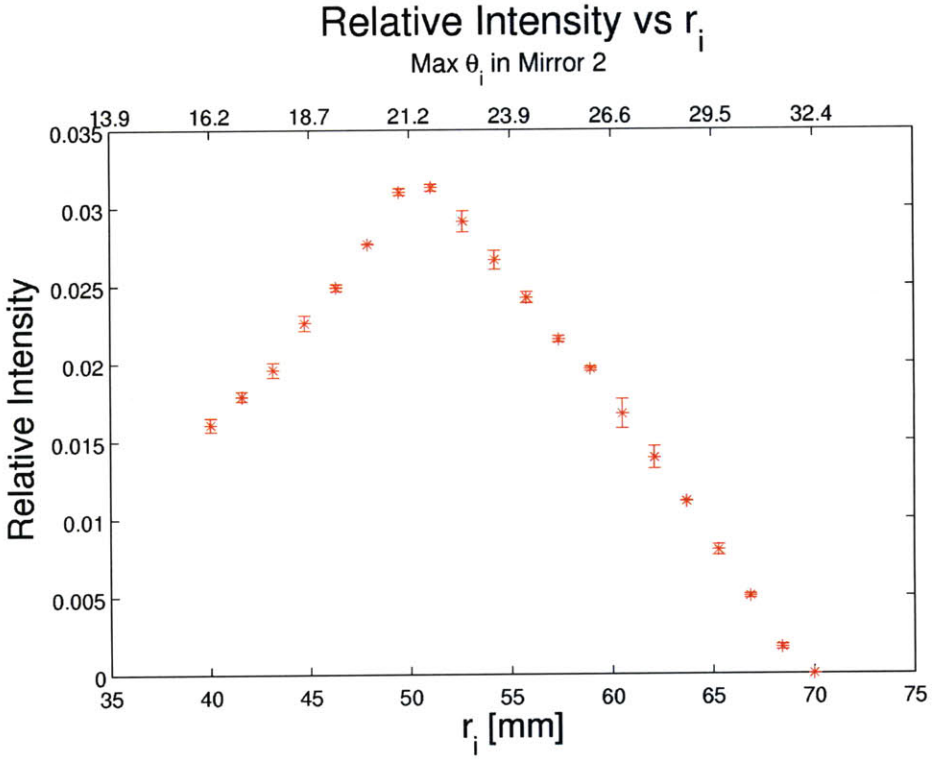

Figure 3-2: Relative flux detected at focal spot for $L = 10$ m, $M = .1$, $r_{source} = 5$ mm system as a function of r_i. Effective cross-section of the mirror bounded by critical angle $\theta_m \approx 21$ mrad in Mirror 2 (hyperboloid).

3.2.1 Effective Cross-Section of Single Mirror System

For a given M and L, flux density at the focal spot was measured as a function of mirror radius r_i. Generally, we expect the effective cross-section of the mirrors, and therefore the flux delivered to the focal spot, to increase with r_i. In the simulation, we observe that this is the case until the grazing angle θ_i reaches the critical angle

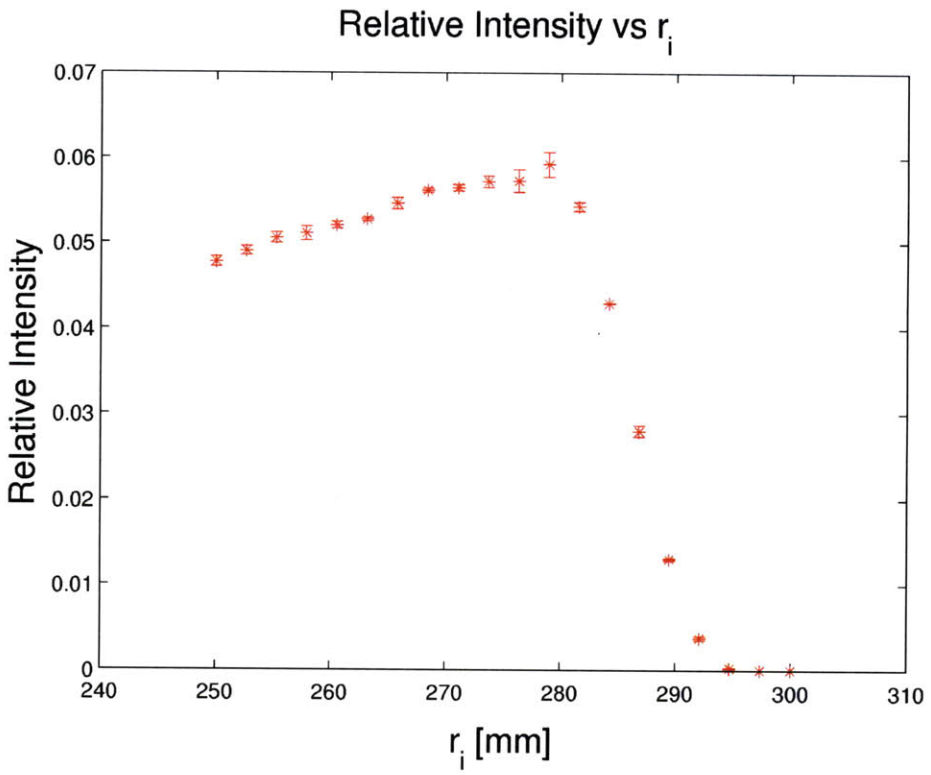

Figure 3-3: Relative flux detected at focal spot for $L = 10$ m, $M = .3$, $r_{source} = 5$ mm system as a function of r_i. Effective cross-section of the mirror bounded by beam radius $r_{beam} = 284$ mm at Mirror 1 (ellipsoid).

($\theta_m \approx 21$ mrad for 5 meV neutrons) or until the entrance radius of the ellipsoid begins to exceed the beam radius at the ellipsoid entrance. Fig. 3.2 shows the case bound by the critical angle for a $L = 10$ m, $M = .1$ system. Here the sharp drop in flux can be fully attributed to the critical angle in the hyperboloid, as r_i is 12 cm below the beam radius at the ellipsoid. Fig. 3.3 shows the case bound by beam radius ($r_{beam} = 284$ mm) for a $L = 10$ m, $M = .3$ system, where θ_i never exceeds 14 mrad.

3.2.2 Flux Density and Magnification

Fig. 3.4 shows the flux density for system lengths $L = 10$ m and $L = 25$ m as a function of magnification, where each case $.03 < M < .9$ untilizes the optimal radius r_i. The largest difference in flux density between the 25 m and 10 m system occurs when $.1 \leq M \leq .4$ but converges to nearly identical values for magnification below that range. The difference in collection is attributed to the decrease in the effective

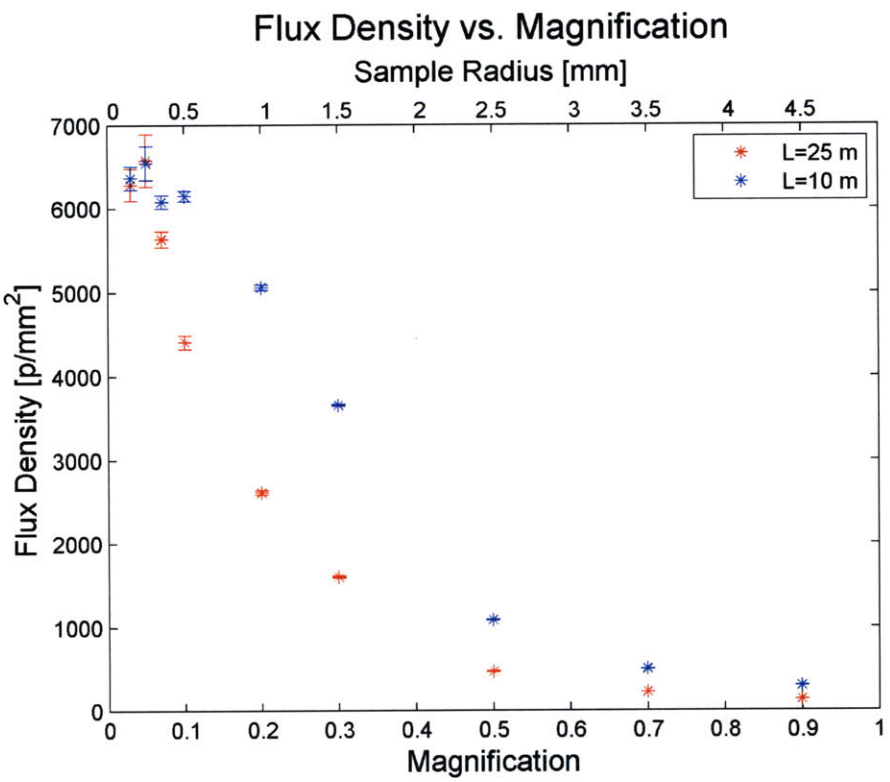

Figure 3-4: Flux density detected at focal spot for $L = 10$ m and $L = 25$ m systems as a function of magnification $M.r_{source} = 5$ mm.

cross-section with increasing distance from the source. Although both cases exhibit a sharp decrease in total flux for $M < .3$, flux density is maximal in this range, clearly showing that the lowest magnification is favorable. From Fig. 3.4 it can be seen that for our given source size of 5 mm, submillimeter samples will receive the most flux density from Wolter mirrors. However, as long as the flux density is uniform across the sample, for a given M, we can vary the size of the source to produce the image size of choice.

3.2.3 Flux Density and Source Size

Fig. 3.5 shows the flux density at the focal spot as a function of source radius for $M = .3$ and $M = .1$. The flux density is shown to stay nearly uniform for sources $1 - 10$ mm in radius, demonstrating the near-absence of off-axis aberration. For the case of $M = .3$, an increase in source size from 1 mm to 10 mm (an increase in sample

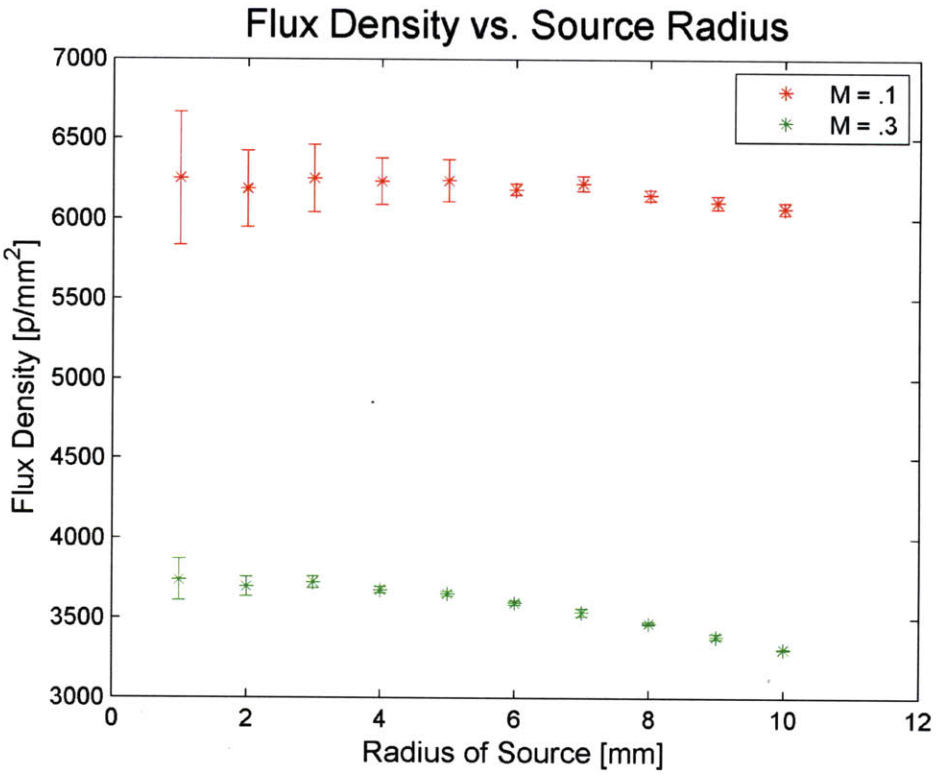

Figure 3-5: Flux density detected at focal spot as a function of source radius for $L = 10$ m systems of $M = .1$ and $M = .3$.

size from .3 mm to 3 mm) would cost about 450 p/mm^2 in flux density. For $M = .1$, the same increase in source size (.1 mm to 1 mm in sample size) would cost about 150 p/mm^2 . This indicates that at least for small sample sizes (< 1 mm in radius), the smallest magnification is preferred. It is possible that in using systems of small M to achieve larger spot sizes (> 3 mm), too much aberration might occur due to the necessarily large source. In this case, a system with a large M and a smaller source might actually yield higher flux on the sample.

3.3 Nested Mirrors

Though finding the optimal radius of single mirrors maximizes their collective power, most of the flux from the source escapes the cross-section of the single mirror, as can be seen from the area of the curve in Fig. 3.2. However, this flux can be recovered by way of nesting several mirrors of identical length and magnification within and

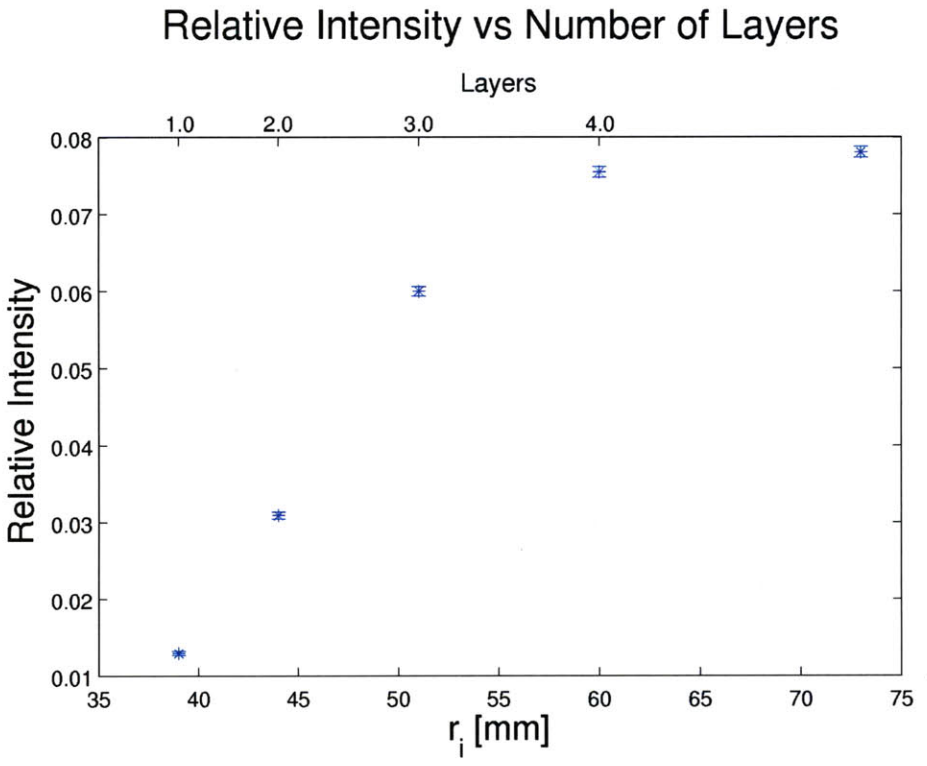

Figure 3-6: Relative intensity detected at focal spot with the addition of mirrors for $L = 10$ m, $M = .1$ nested system.

outside the optimal radius. The fact that Wolter Type I mirrors are full figures of revolution make them easy to nest in this way. Fig. 3.6 shows the increase in relative flux at the focal spot with the addition of each mirror to the $M = .1$, $L = 10$ m system. Plotting the individual contributions to the relative intensity from each layer (Fig. 3.7) we can show that after adding only 4 layers to the system, all available flux is collected, producing a flux density of $15,300$ p/mm^2 at the focal spot.

3.4 Case with No Optics

The set-up for the no optics case consisted of a source and a detector 200 mm apart, and two pinholes, one placed at the source and the other placed at the detector. The pinhole at the detector serves to define the sample size ($r = .05$ mm to 1 mm) while the pinhole at the source absorbs any unused portion of the beam by the sample. The

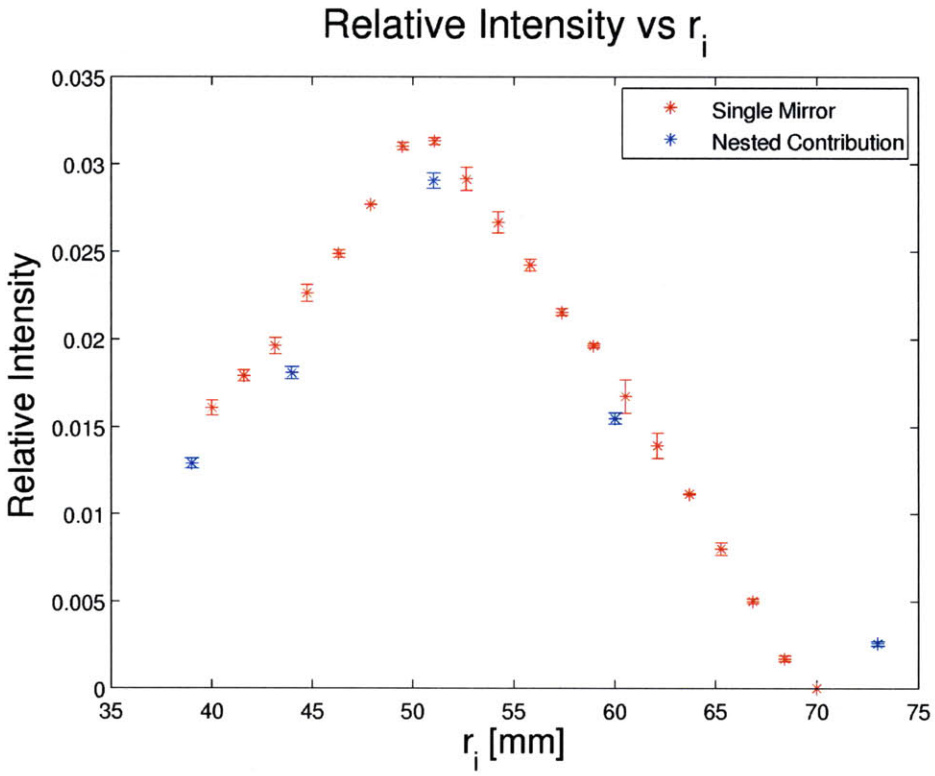

Figure 3-7: Contributions to relative intensity at focal spot from individual mirrors in nested system (blue) superimposed over collection from single-mirror system as a function of r_i (red). Both are $L = 10$ m, $M = .1$ systems.

radius of the pinhole at the source is

$$r_{pinhole} = D \tan \theta_{div} + r_{sample} \tag{3.2}$$

where the distance between the source and detector is $D = 200$ mm and the maximum divergence of the source is $\theta_{div} = 1$ degree. For the given parameters of this test, source size places no restrictions on the flux reaching the sample, and maximum acceptance of the sample is always achieved. For $r_{pinhole} = 12.7$ mm the uniform flux density at the sample was measured as a function of sample radius. As expected, the flux density remains uniform across the sample at about 2000 p/mm^2. Comparing this to the flux density of $15,300$ p/mm^2 delivered by the $M = .1$, $L = 10$ m nested system, we see the relative effectiveness of the Wolter Type I microscope as a focusing device.

Chapter 4

Simulation of Surface Errors

Typically, polished optical surfaces exhibit two types of surface error that affect the quality of the image at the focal spot. One type, associated with large, slowly-varying deformations of the ideal surface profile, are called figure errors. The second type, associated with small, high-frequency deviations arising from surface roughness, are called finish errors. Both errors depend highly on the manufacturing and polishing process and are specific to each set of mirrors produced. Therefore, though the analysis of errors in this chapter can be generalized to like surfaces, this analysis will be applied specifically to the set of four mirrors used in the experiment at MIT described in the next chapter.

4.1 Figure Errors

4.1.1 Slope Errors

During the manufacturing of the mirrors, deviations from the ideal profile, known as figure errors or slope errors, occur in the mirror. Figure errors alter the trajectory of reflected neutrons, leading to a distortion of the focal spot. The height deviations are large compared to the wavelengths of the neutrons and change slowly along the length of the mirror (large spatial periods) so that the effect on trajectory is purely geometric. Though figure errors occur both axially (along the z-axis) and radially

(along the azimuthal angle), in Wolter-type geometries, the radial error contributions to the distortion of the focal spot are small compared to the axial contributions. A recent discussion of radial vs. axial errors for a Wolter I telescope gives a quantitative comparison (Chon, Namba, and Yoon, 2007)[1]. The curve of the height deviations $\Delta r(z)$ for the hyperboloid surface is plotted in Fig. 4.1, where ranges from $-.2 < \Delta r(z) < .7$ μm, experiencing a maximum at the edges of the mirror. The continuous curve in Fig. 4.1 is a cubic spline interpolation of discrete data points measured from the surface. Including the height deviations, the equation describing the hyperboloid

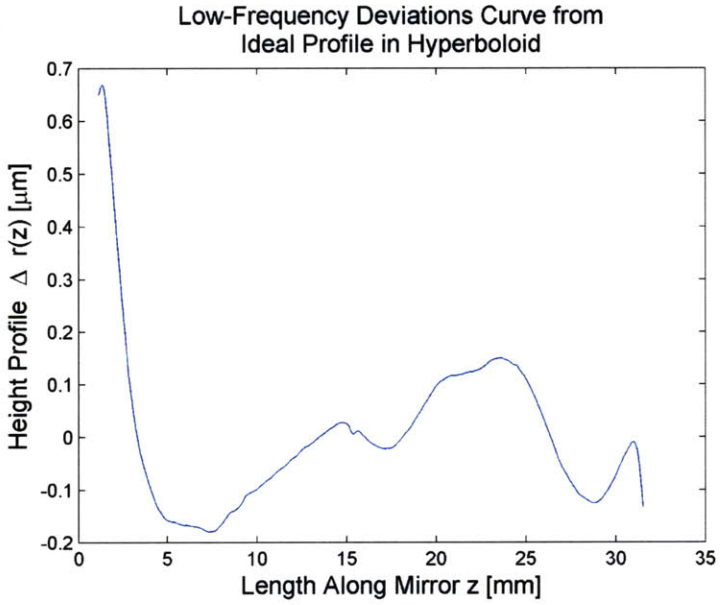

Figure 4-1: Low-frequency hieght deviations Δr(z) from ideal profile in hyperboloid along mirror length z.

surface becomes

$$F'(z, r, \Delta r(z)) = b^2(z - z_0)^2 - a^2(r + \Delta r(z))^2 - a^2b^2 = 0 \tag{4.1}$$

with the new surface normal $\vec{n}'$

$$\vec{n}' = \nabla F' = \vec{n} + \Delta\vec{n} = \begin{pmatrix} -a^2x \\ -a^2y \\ -b^2(z - z_0) \end{pmatrix} + \begin{pmatrix} 0 \\ 0 \\ -a^2(r + \Delta r(z))\frac{\partial \Delta r}{\partial z} \end{pmatrix} \tag{4.2}$$

The change in the grazing and reflecting angle $\Delta\theta$ is then the angle between $\vec{n}$ and $\vec{n}'$ and can be calculated for every point along the surface of the mirrors.

4.1.2 Spatial Errors

In addition to errors in slope, there are the height deviations themselves. If taken into account, the height deviations make the neutron ray appear to be coming from a shifted point on the source, which consequently correspond to a positional shift in focal spot. However, the poisitional shifts in the focal spot due to the slope errors alone greatly dominate the positional shifts from the height deviations. We can show this by first translating the hight deviation Δr into a displacement $\Delta z_1 + \Delta z_2$ along the ideal surface as shown in Fig. 4.2. The shift Δz_2 correponds to an arbitrary shift of the perturbed surface function to an intersection point with the incident ray. The reflected ray is then identified with ray 2 instead of ray 1. Tracing ray 2 back to where it intersects the ideal surface results in an additional shift Δz_1 for the intersection point, which in turn corresponds to a shift of the ray's origin at the source. By shifting the point of reflection by $\Delta z_1 + \Delta z_2$, we've completely incorperated the spatial surface errors into a shift in the ray's origin at the source that directly maps to a positional shift in the focal plane. For grazing incidence, we can estimate the maximum position shift at the source to be $\approx \Delta r$ which is on the order of 10^{-4} mm. In light of this argument, we assume that distortions to the focal spot from the spatial part of the figure errors are neglible. The relative intensity of neutrons that scatter at an angle $\Delta\theta_s$ from the incident angle from slope errors in the hyperboloid are shown in Fig. 4.3. We find that $|\Delta\theta_s| < .1$ mrad which suggests that the effect of figure errors on imaging is small. The effect will be discussed together with the effect of finish errors in the next section.

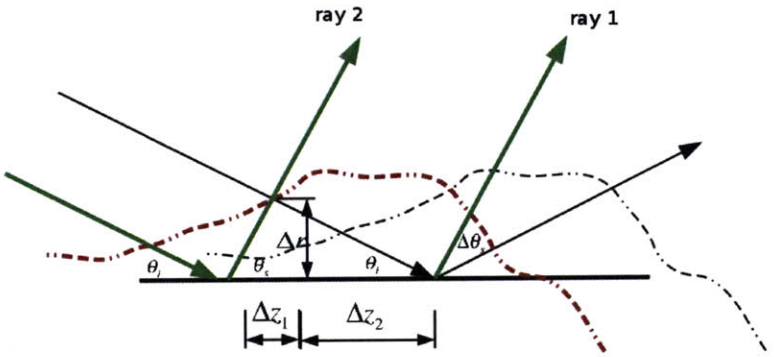

Figure 4-2: Translation of height error Δr to displacement $\Delta z_1 + \Delta z_2$ of ray along the ideal surface.

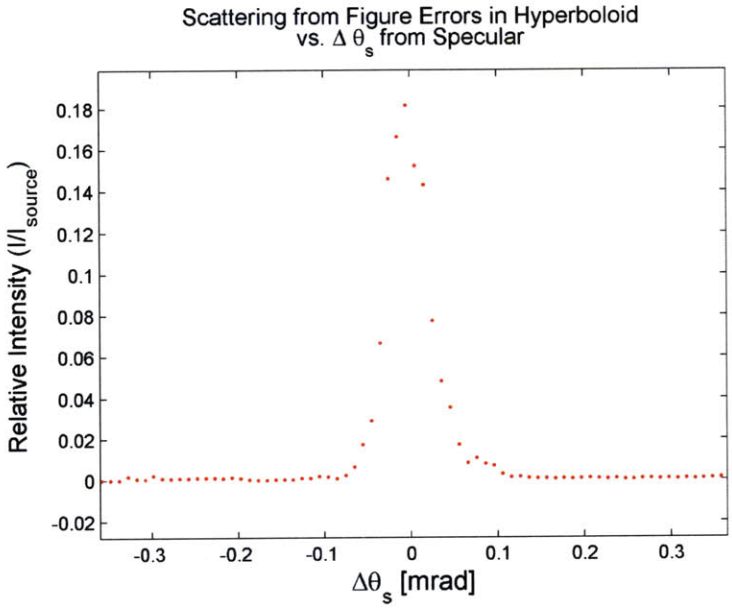

Figure 4-3: Relative intensity of neutrons that scatter at an angle $\Delta\theta_s$ from the specular due to slope errors in the hyperboloid mirror.

4.2 Simulation of Error due to Surface Roughness

4.2.1 Scattering from Sinusoidal Grating using Rayleigh-Rice Theory

Diffraction-like scattering occurs when the deviations from the ideal profile of a surface are comparable to the projected wavelength of the scattered beam. In this case reflected beams of the same wavelength and incident angle will interfere due to the

path length differences introduced by the surface height deviations. For the simple case of a one dimensional reflective sinusoidal grating shown in Fig. 4.4, the height deviation is

$$h(z) = a\sin(2\pi f_g z + \alpha) \tag{4.3}$$

where a is the amplitude, α is an arbitrary phase, and

$$f_g = \frac{1}{\Lambda} \tag{4.4}$$

The angles of scattering from the surface plane of frequency f_z are given by the

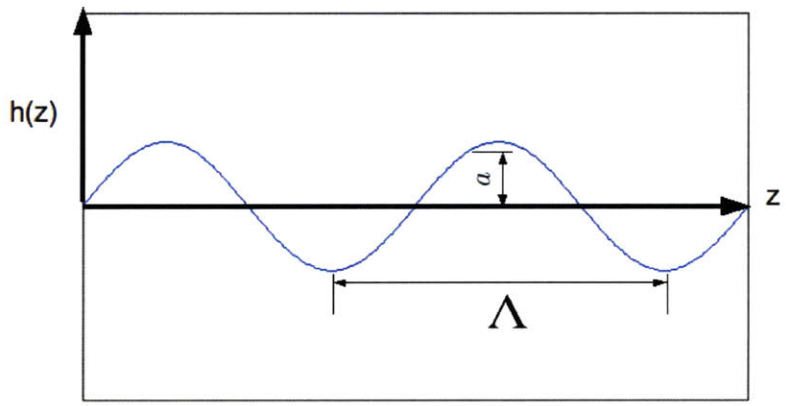

Figure 4-4: Sinusoidal grating surface $h(z) = a\sin(2\pi f_g z + \alpha)$ of amplitude a, spatial period Λ, and spatial frequency $f_g = \frac{1}{\Lambda}$.

grating equation

$$\cos(\theta_n) - \cos(\theta_i) = n f_z \lambda \quad n = 0, \pm 1, \pm 2... \tag{4.5}$$

where λ is the neutron wavelength, θ_i is the angle of incidence, and the scattering angle θ_n corresponds to the n^{th} order of diffraction. For a smooth surface, contributions to orders above $n = \pm 1$ are negligible and scattering is dominated by the $n = 0$ specular order and $n = \pm 1$ orders. Thus for a smooth sinusoidal surface of frequency f_g, there will be two off-specular directions in addition to the specular through which neutrons of a particular wavelength and angle of incidence will scatter. Generally, the fraction of incident neutrons that scatter into a solid angle Ω_s is obtained by integrating the

bidirectional scatter distribution function (BSDF):

$$\frac{dI_s}{I_i} = BSFD(\theta_i, \lambda, \theta_s) \sin\theta_s d\Omega_s \tag{4.6}$$

Here, $\sin\theta_s$ is a geometric obliquity factor where θ_s is the scattering angle. For the case of a smooth and clean (defect-free) surface, the BSFD is derived using Rayleigh-Rice vector perturbation theory [6]. In the one dimensional case, Rayleigh-Rice theory yields the equation

$$\frac{1}{I_i}\frac{dI_s}{d\theta_s} = \frac{16\pi^2}{\lambda^3} \sin\theta_i \sin^2\theta_s \sqrt{R_F(\theta_i)R_F(\theta_s)} S(f_z) \tag{4.7}$$

where $R_F(\theta_i)$ and $R_F(\theta_s)$ are the incident and specular Fresnal reflectivity curves for zero roughness and $S(f_z)$ is the power spectral density function in terms of the spatial frequency. The PSD function of a surface profile $h(z)$ of length L is defined as

$$S(f_z) = \lim_{L\to+\infty} \frac{1}{L}|Z(f_z, L)|^2 \tag{4.8}$$

where $Z(f_z, L)$ is the fourier transform of $h(z)$ into the frequency domain and is given by

$$Z(f_z, L) = \int_{-L/2}^{L/2} h(z) e^{-i2\pi f_z z} dz \tag{4.9}$$

Integrating $S(f_z)$ over all present frequencies would thus yield the average "roughness energy" per length,

$$\sigma^2 = \int_{-\infty}^{\infty} S(f_z) df_z \tag{4.10}$$

or average "roughness power" of the surface σ^2. For the sinusoidal grating in (4.3), the power of the surface is contained entirely in a single frequency, the spatial frequency f_g of the grating. The PSD function is then accordingly

$$S(f_z) = \frac{a^2}{4}[\delta(f_z - f_g) + \delta(f_z + f_g)] \tag{4.11}$$

resulting in a non-zero intensity at the scattering angles

$$\theta_{g\pm} = \arccos(\cos\theta_i \pm f_g\lambda) \tag{4.12}$$

Assuming reflectivity of unity, we integrate (4.7) over all frequencies and find that the fraction of incident neutrons scattering into the first diffraction orders is

$$\frac{I_{\pm 1}}{I_i} = \left(\frac{2\pi a}{\lambda}\right)^2 \sin\theta_i \sin\theta_{g\pm} \tag{4.13}$$

Rewriting this in terms of the momentum transfer of the specular and scattered beams

$$\begin{aligned} q_i &= \frac{4\pi \sin\theta_i}{\lambda} \\ q_s &= \frac{4\pi \sin\theta_s}{\lambda} \end{aligned} \tag{4.14}$$

and the total roughness squared σ^2 we have

$$\frac{I_{\pm 1}}{I_i} = \frac{\sigma^2}{2} q_i q_{g\pm} \tag{4.15}$$

However, the fractions in (4.15) do not add to unity. This is because (4.7) only describes the fraction of neutrons scattered diffusely and does not account for the specularly scattered portion. Since flux is conserved, we expect the fraction scattered into the specular to be approximately $1 - I_+/I_i - I_-/I_i$. That is, we expect the fractions scattered specularly and diffusely to add to one. In general, upon the introduction of roughness, the flux reflected into the specular will be modified by an exponential factor known as the Debye-Waller factor [5]. The resulting specular reflectivity is then

$$\frac{I_{spec}}{I_i} = R_F(\theta_i)\exp(-\sigma^2 q_i^2) \tag{4.16}$$

Taking $R_F(\theta_i)$ to be unity and expanding the exponent in (4.16) up to the linear term, the fraction of specularly scattered neutrons becomes

$$\frac{I_{spec}}{I_i} \approx 1 - \sigma^2 q_i^2 \approx 1 - \sigma^2 q_i q_s \tag{4.17}$$

if $\sin\theta_i \approx \sin\theta_s$. Thus, we find that the fraction scattered diffusely (4.15) and the fraction scattered specularly (4.17) add to one as long as deviations from the specular are small and $\sigma^2 q_i^2 \ll 1$. The latter condition is known as the Rayleigh-Rice criterion for smooth surface scattering and is the condition for which (4.7) is consistent with (4.15).

4.2.2 Scattering from a Fractal Surface

A polished, isotripic surface can be thought of as an infinite sum of sinusoids that span a continuous range of spatial frequencies and amplitudes. Typically, an optically-polished surface exhibits a fractal surface structure whose PSD is modeled by power-law function:

$$S(f) = \frac{C}{f^\alpha} \tag{4.18}$$

where the index α is real and spans $1 < \alpha < 3$ and C is a normalization factor. Fig. 4.5 shows a plot of the power-law PSD that Willingale uses to model the surface of an electroless nickel plated, gold-coated Wolter-Schwarzwild Type I wide field camera mirror [7]. Willingale's combined measurements of the surface estimate C to lie within the range $2410 - 4455$ and $\alpha = 2.41$, where the PSD function itself is in units of $\mathring{A}^2$ mm and the frequency is in mm^{-1}. For the rest of his discussion, he uses 3000 for C, which is also what I will do here. Additionally, I halve C whenever the PSD function is two-sided, meaning that it is a function of both negative and positive frequencies, as it is in Fig. 4.5. As with the single frequency grating, the positive frequencies map to scattering angles $\theta_s < \theta_i$, while the negative frequencies map to $\theta_s > \theta_i$.

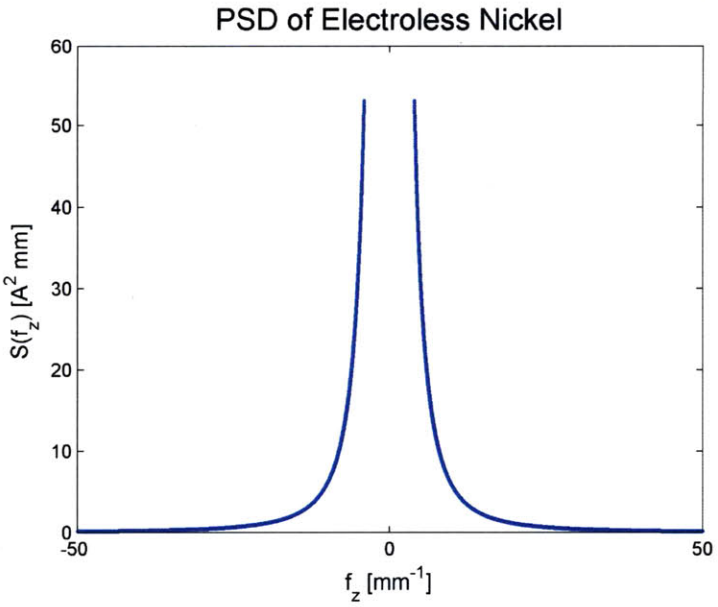

Figure 4-5: Power-law PSD function with $C = 3000$, $\alpha = 2.41$, for the frequency range $f_{min} = 4$ mm $^{-1} < |f_z| < f_{max} = 50$ mm $^{-1}$.

Choosing the Frequency Range for the BSDF

Let us rewrite the BSDF in (4.7) in terms of f_z, q_i, and $q_s(f_z)$

$$\frac{1}{I_i}\frac{dI_{diff}}{df_z} = q_i q_s(f_z)\sqrt{R_F(q_i)R_F(q_s(f_z))}S(f_z) \tag{4.19}$$

and let us integrate over all spatial frequencies to find the total fraction of neutrons that scatter away from the specular

$$\frac{I_{diff}}{I_i} = q_i\sqrt{R_F(q_i)}\int_{-\infty}^{\infty}\sqrt{R_F(q_s(f_z))}q_s(f_z)S(f_z)df_z \tag{4.20}$$

The power-law PSD function is perfectly symmetric around $f_z = 0$ but has a singularity which causes the integral in (4.20) to diverge in the near-zero frequency range. However, according to the grating equation, the singularity at $f_z = 0$ corresponds to scattering into the specular beam. Likewise, near-zero frequencies correspond to figure errors of long spatial period rather than surface roughness. Consequently, this low frequency range must be excluded from the range of integration in (4.20). To define a reasonable division between the figure error and finish error range, we look at

the fourier transform of the measured surface profile which includes figure error (Fig. 4.6). In both the Ellipsoid and Hyperboloid profiles, the maximum present frequency was found to lie in the 3 mm^{-1} to 10 mm^{-1} range and 4 mm^{-1}. Consequently the minimum frequency contributing to finish errors was chosen to $f_{min} = 4$ mm^{-1}.

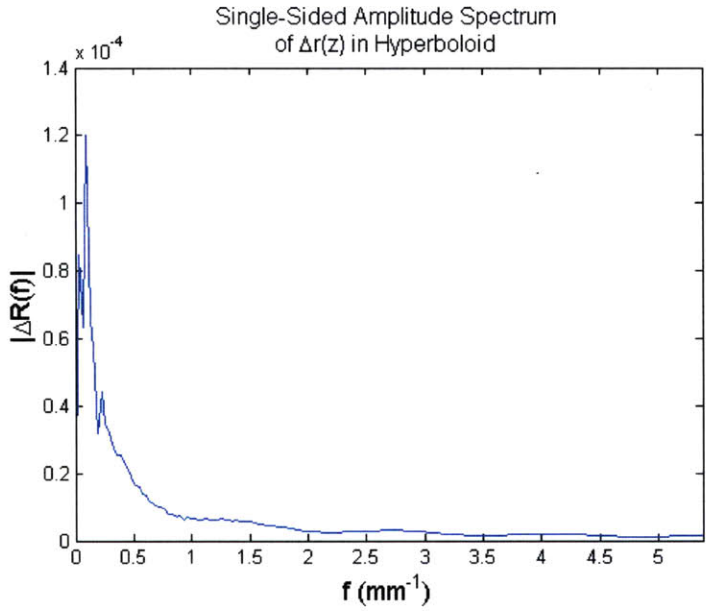

Figure 4-6: Fourier-Transform $|\Delta R(f)|$ of the error in the surface profile $\Delta r(z)$ of the hyperboloid mirror.

For positive frequencies, the upper limit of integration f_{max} is bound by the minimum scattering angle $\theta_s = 0$ that corresponds to scattering along the plane of the surface. Fig. 4.7 shows the relationship between the angle of incidence θ_i and that frequency which corresponds to scattering in the $\theta_s = 0$ direction. The plot shows the cases for neutron wavelengths $\lambda = 4, 6$, and 8 $\AA$ in the frequency range $50 - 120$ mm^{-1} where the curves of θ_i for $\lambda = 4$ $\AA$ and $\lambda = 6$ $\AA$ are truncated at the respective critical angles. The dotted horizontal line indicates the maximum grazing angle (10 mrad) that occurs for the mirrors as determined by the ray-tracing simulation. From the curves it is estimated that the maximum frequency that contributes to scattering above the surface the plane for $\theta_i < 10$ mrad is ≤ 90 mm^{-1} for all neutron wavelengths. Though the surface plane provides an absolute upper limit to the maximum frequency f_{max}, contributions to (4.20) from $f_z < f_{max}$ may still be small enough to ignore. If the Rayleigh-Rice criterion $\sigma^2 q_i^2 \ll 1$ is satisfied, we know from (4.16)

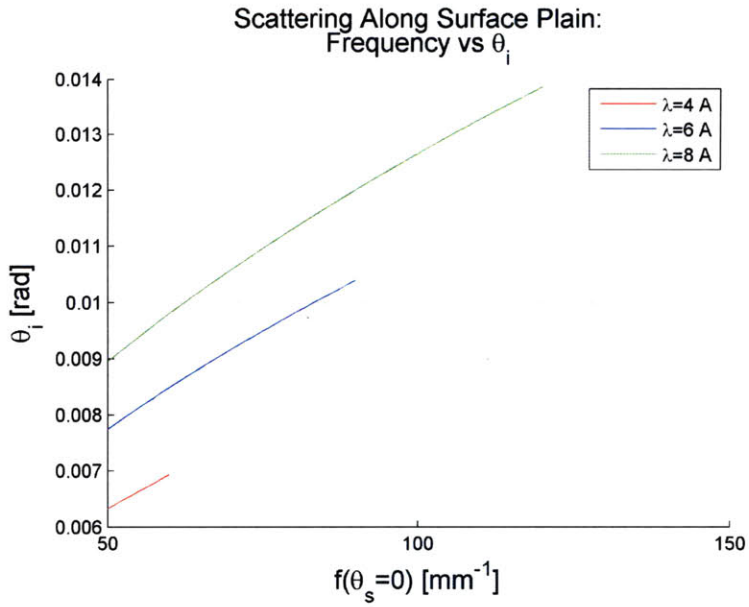

Figure 4-7: Relationship between maximum spatial frequency that contributes to scatteing above the surface plane and the angle of incidence θ_i. The three curves are for neutron wavelengths $4, 6$, and 7 $\mathring{A}$. The dotted line is the maximum occuring grazing angle in the mirrors for our experiment.

that the contribution from the frequency range $f_{min} < f_1 < f_z < f_2$ to our diffusely scattered fraction in (4.20) is

$$\frac{\Delta I_{diff}}{I_i} = \exp(\sigma^2(f_1)q_i^2) - \exp(\sigma^2(f_2)q_i^2) \tag{4.21}$$

where $\sigma^2(f')$ is just our PSD (4.18) integrated from f_{min} to f'

$$\sigma^2(f') = \int_{f_{min}}^{f'} S(f_z)df_z = \frac{C}{(\alpha-1)}\left[\frac{1}{f_{min}^{(\alpha-1)}} - \frac{1}{f'^{(\alpha-1)}}\right] \tag{4.22}$$

Fixing f_1 and f_2, we can plot $\Delta I_{diff}/I_i$ as a function of θ_i. This is done in Fig. 4.8 for case $f_1 = 50$ mm^{-1} and $f_2 = 90$ mm^{-1} from which we find that the maximum contribution of the range $f_1 < f_z < f_2$ to the fraction of diffusely scattered neutrons is $< .25\%$. Comparing this to the total contribution from all frequencies $f_z > f_{min}$ (Fig. 4.9), we find that the maximum relative error $\Delta I_{diff}/I_{diff}$ introduced by neglecting the frequencies is 2.2% and occurs for the lower angles of incidence (Fig. 4.10). Calculating $\Delta I_{diff}/I_{diff}$ for lower values of f_1, it was determined that the total

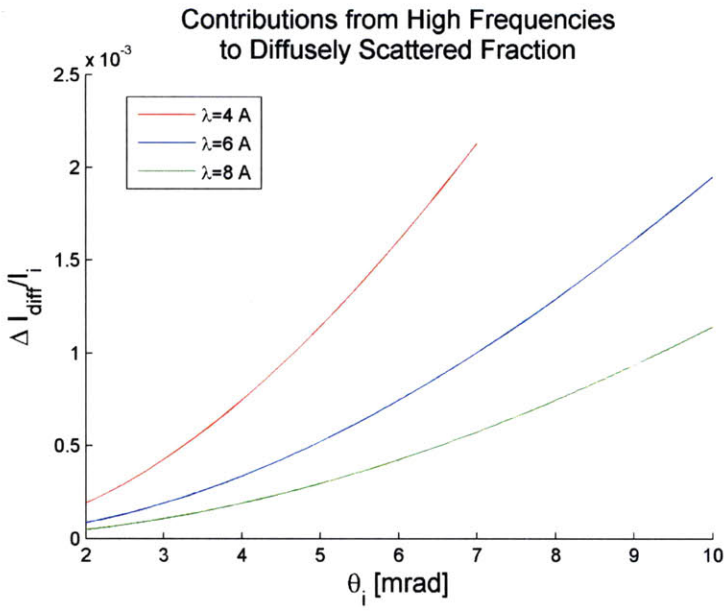

Figure 4-8: Contributions for the frequencies $50 - 90$ mm^{-1} to the diffusely scattered fraction $\Delta I_{diff}/I_i$ for neutron wavelengths $4, 6$, and $7\mathring{A}$.

integral in (4.20) is insensitive to the upper limit f_{max} for values as low as 35 mm^{-1}, introducing errors $< 5\%$ into the diffusely scattered fraction. All things considered, we choose $f_{max} = 50$ mm^{-1} so as to keep the error below 2.2%. Thus (4.20) becomes

$$\frac{I_{diff}}{I_i} = q_i\sqrt{R_F(q_i)}\left[\int_{-f_{max}}^{-f_{min}} \sqrt{R_F(q_s(f_z))}q_s(f_z)S(f_z)df_z + \int_{f_{min}}^{f_{max}} \sqrt{R_F(q_s(f_z))}q_s(f_z)S(f_z)df_z\right] \tag{4.23}$$

where $f_{min} = 4$ mm^{-1} and $f_{max} = 50$ mm^{-1}.

Rayleigh-Rice Criterion: Constraints on Wavelength and Angle of Incidence

The criterion for (4.23) is the Rayleigh-Rice criterion $\sigma^2 q_i^2 << 1$ which allows the first-order approximation in (4.17). Fig. 4.11 plots $\sigma^2 q_i^2$ (a) and the second-order correction $\sigma^4 q_i^4/2$ (b) for $0 < \theta_i < 10$ mrad for our chosen frequency range. For the given range in θ_i, the second-order corrections never exceed .01 or 1% of the total scattering. To see the effect of this correction on (4.23), we plot $I_{spec}/I_i + I_{diff}/I_i$ without the second-order correction in Fig. 4.12a and then with a rough version of it

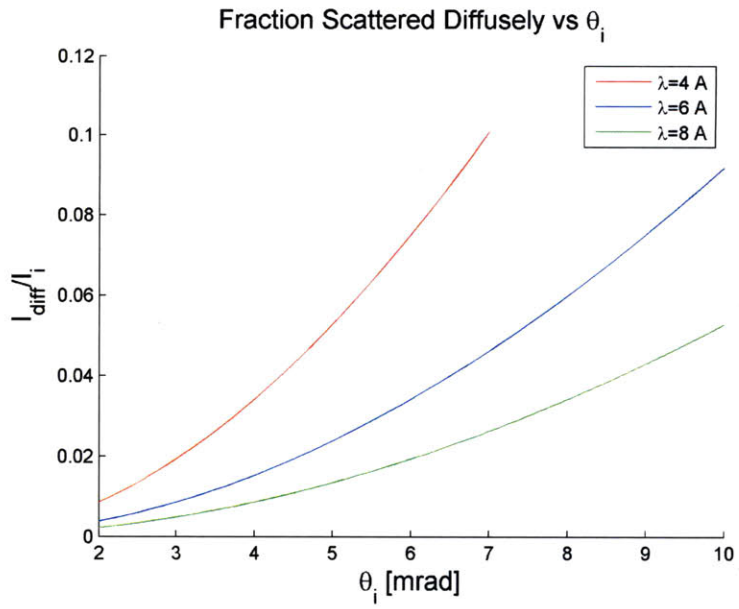

Figure 4-9: The total diffusely scattered fraction I_{diff}/I_i as a function of incident angle θi for all frequencies $f_z > f_{min}$.

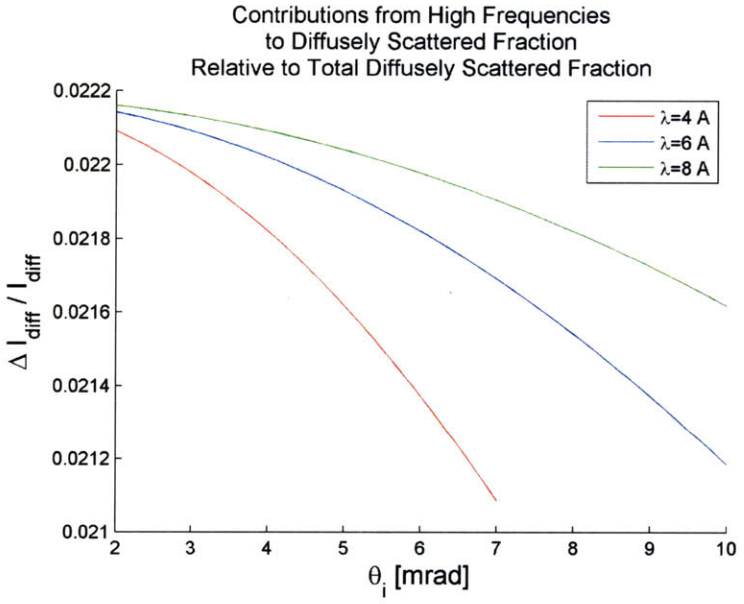

Figure 4-10: Fraction of diffusely scattered flux due to spatial frequencies $50 - 90$ mm^{-1}. The red, blue, and green curves are for neutron wavelengths $4, 6$, and $7\mathring{A}$ respectively.

in Fig. 4.12b, where the correction amounts to subtracting $\sigma^2 q_i^2$ from I_{diff}/I_i. With the correction in place, we see that the maximum error in (4.23) for the given range in θ_i reduces to .2%. However, accounting for the correction in the non-integrated

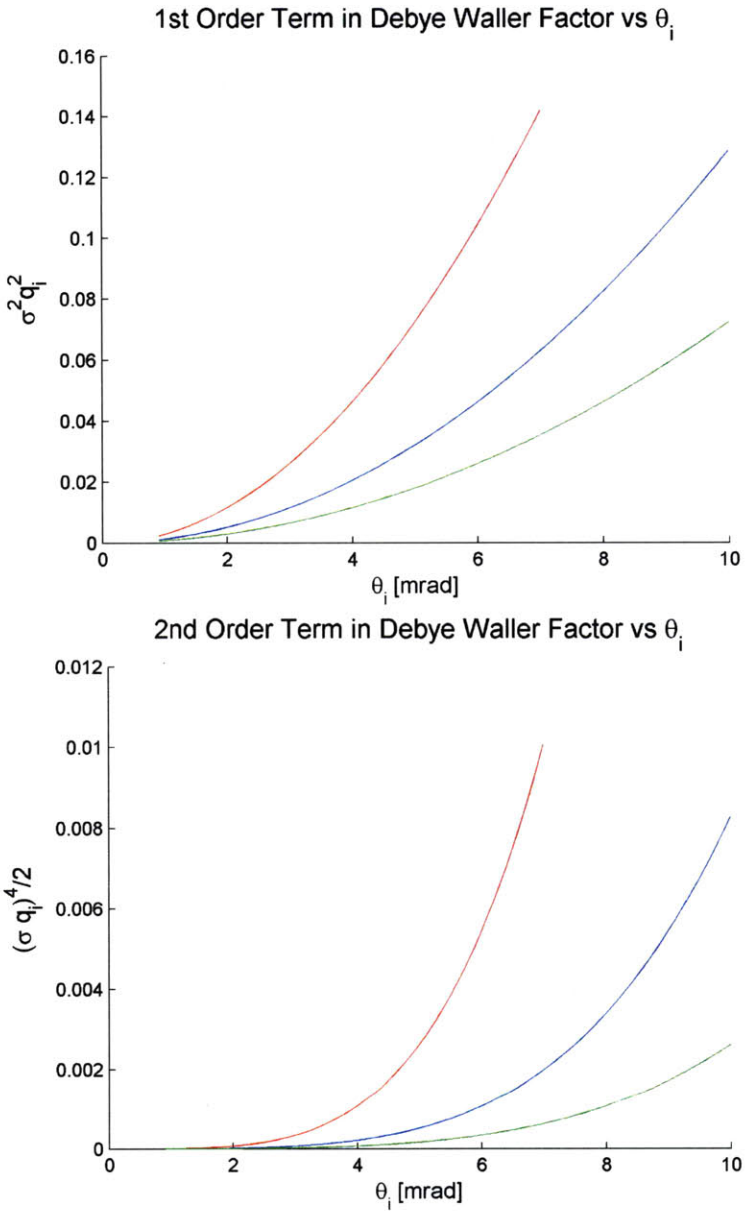

Figure 4-11: First (a) and second order (b) term in the Debye Waller factor as a function of incident angle for frequencies $4 < f_z < 50$ mm^{-1}. The red, blue, and green curves are for neutron wavelengths $4, 6$, and $7\mathring{A}$ respectively.

BSDF in (4.20) is complicated and makes the application of the equation in the simulation more difficult. Since the maximum error in the first-order approximation is only 1%, we choose to apply (4.20) without correction, keeping in mind that error will increase for mirror geometry with larger angles of incidence and larger critical angles that reflect neutrons of shorter wavelengths. In addition to this, corrections

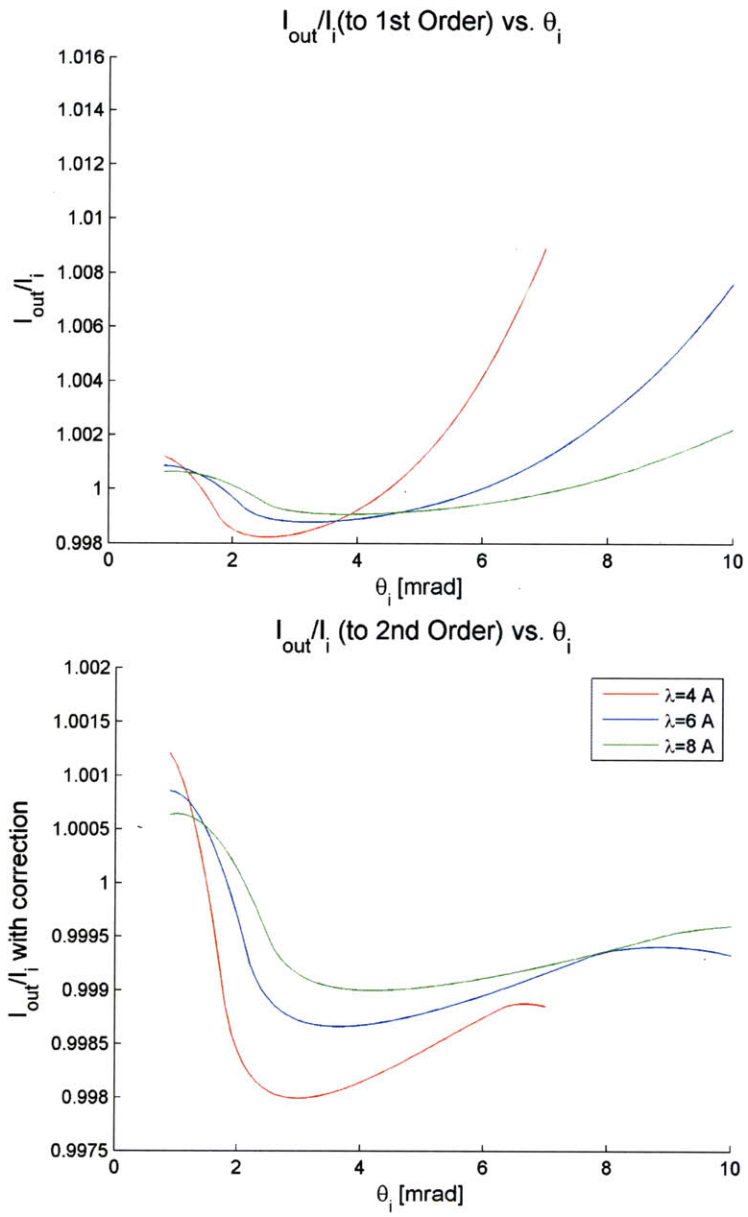

Figure 4-12: First (a) and second order (b) approximations of the total fraction of scattered flux due to both figure and finish errors as a function of incident angle.$4 < f_z < 50$ mm^{-1} and the red, blue, and green curves are for neutron wavelengths $4, 6$, and $7\mathring{A}$ respectively.

for second-order ($m = \pm 2$) diffraction become present for $\sigma^2 q_i^2 \approx 1$, but are less than .1% [6].

4.2.3 Simulating Diffuse Scattering with the BSDF

The sine-corrected BSDF in (4.7) is plotted in Fig. 4.13 for Willingale's PSD function in the chosen frequency range $f_{min} = 4$ mm $^{-1} < |f_z| < f_{max} = 50$ mm $^{-1}$. The assymetry of the BSDF is due to the sine obliquity factors and is more pronounced with decreasing θ_i. The empty region around $\Delta\theta_s = 0$ corresponds to near-specular

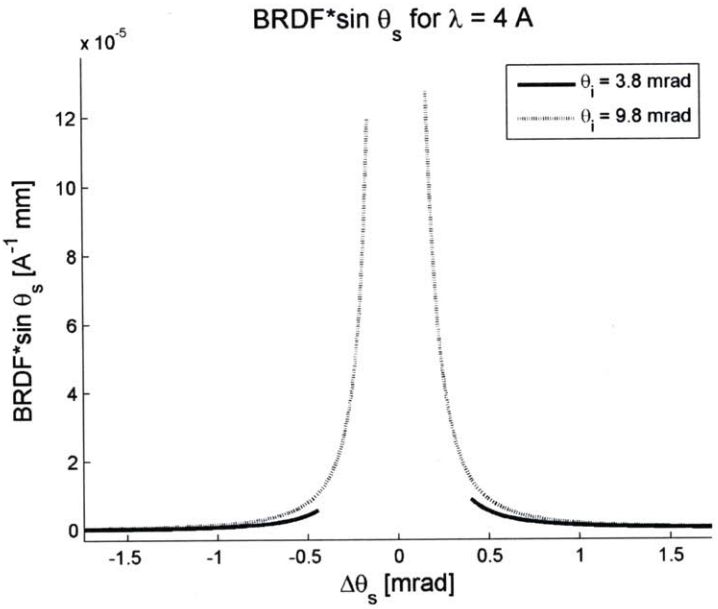

Figure 4-13: Sine-corrected BRDF (BSDF) for a power-law PSD function with parameters $C = 3000$ and $\alpha = 2.41$. $4 < f_z < 50$ mm^{-1}. The solid line corresponds to $\theta_i = 3.8$ mrad while the dotted line corresponds to $\theta_i = 9.8$ mrad.

scattering due to figure errors. As shown in the plot, this region becomes narrower for higher angles of incidence with increasing contributions to diffuse scattering from the lower frequencies. We can compare the calculated distribution in Fig. 4.13 with a histogram of the simulated scattering distribution in Fig. 4.14, which plots the realtive intensity if diffustly scattered neutrons in the Hyperboloid as a function of $\Delta\theta_s$ for all occuring θ_i and $4\mathring{A} < \lambda < 8\mathring{A}$. The simulation results are as what we would expect from Fig. 4.13, with an additional softening of the boundary between figure and finish regions due to varying θ_i and λ. The simulated overlap between scattering due to the figure errors and scattering due to the finish errors in the hyperboloid is shown in Fig. 4.15. The overlap may be made smoother by extending f_{min} of the BSDF to lower frequencies. However, this will increase the roughness σ significantly,

introducing greater error into the Rayleigh-Rice BSDF calculation. Though not ideal, the overlap is sufficient to cover all θ_s between the two regions while keeping the error discussed in the previous section small.

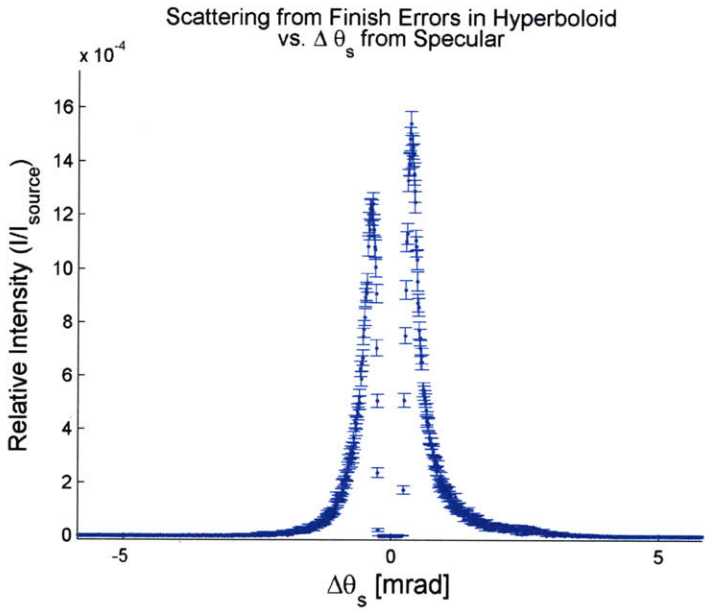

Figure 4-14: Simulation of relative diffusely scattered flux as a function of $\Delta\theta_s$ in the hyperboloid mirror. $4\mathring{A} < \lambda < 8\mathring{A}$ and $\theta_i < 1$.

4.3 Simulating the Effect of Figure Errors and Finish Errors on Focal Spot

The effect of figure and finish errors on the half power diameter (HPD) of the focal spot was simulated for the set-up of the MIT Experiment. To replicate the source from the MIT reactor, a Maxwellian source emmiting neutrons of $\lambda = 1 - 8\ \mathring{A}$ from a $T = 328$ K distribution was placed $2,451$ mm upstream from the first focus where a pinhole ($r = 1$ mm) served to define the focal source. The maximum divergence of the beam was defined by the projection of the 2×3 in Maxwellian window onto the focal source and was approximately 1 deg. The geometric parameters of the 4 nested Ni shells are defined in Table I of Appendix A. The total source to image distance L is 3200 mm while the magnification M is .25.

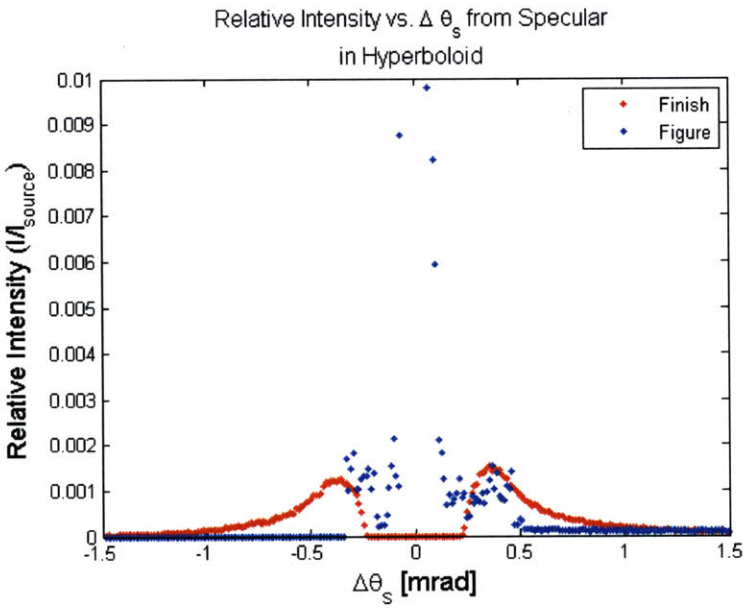

Figure 4-15: Overlap of relative scattering from roughness (red) and figure errors (blue) as a function of $\Delta\theta_s$ in the hyperboloid mirror simulation. $4\mathring{A} < \lambda < 8\mathring{A}$ and $\theta_i < 1$.

Three cases were simulated: one for the ideal mirrors, one for mirrors suffering from figure errors only, and one for mirrors suffering from both figure and finish errors. The azimuthally-integrated focal spots are shown in Fig. 4.16a-b for each case, with half power diameters of .356, .369, and .394 mm respectively where the expected HPD for the no error case is $.5/\sqrt{2} = .354$ mm. The simulated HPD of the third case is significantly lower than the experimentally measured HPD of .7 mm. Most of the additional error is known to come from slight distortions of the shells due to imperfect mechanical fitting of the holder. However, a small change to the finish error contribution to the HPD may arise once the actual PSD of the mirrors is measured and used.

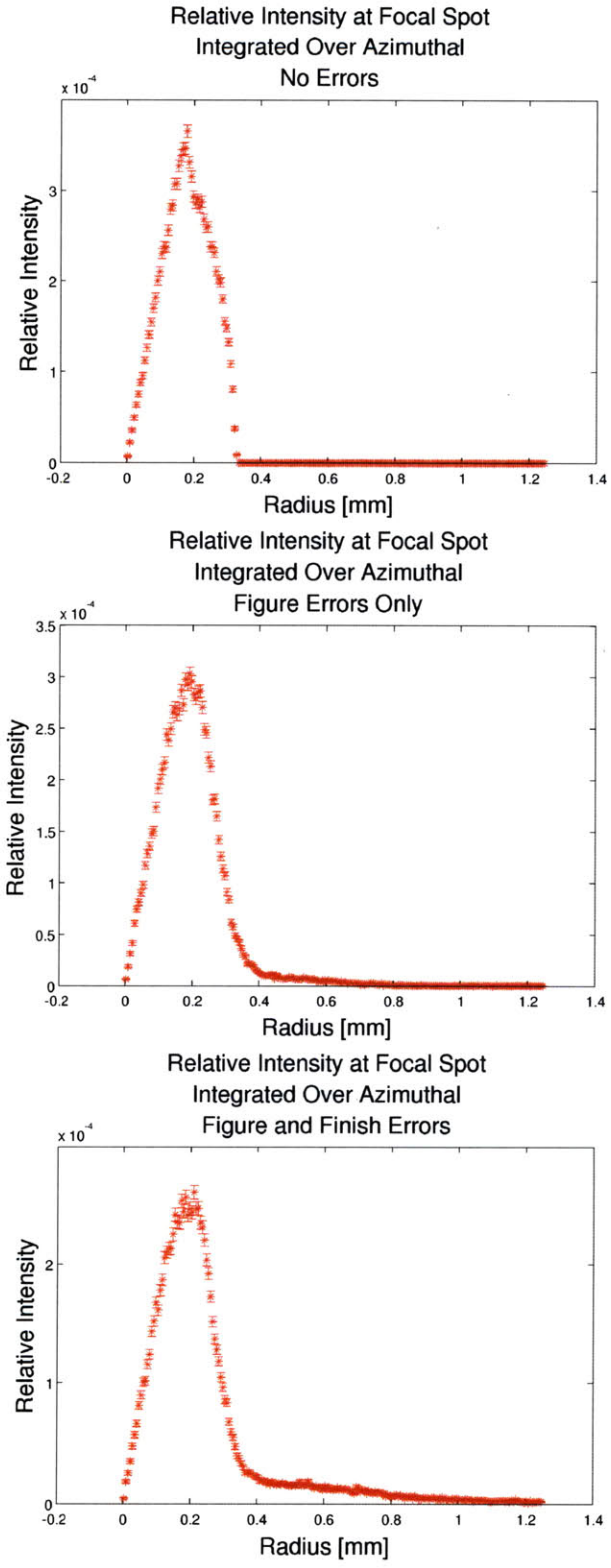

Figure 4-16: Relative intensity at focal spot integrated over azimuthal angle vs. radial postion. (a) is for the no error case, (b) includes the effect of figure errors, and (c) includes both figure and finish errors.

Chapter 5

Testing of Wolter Microscope at MIT Nuclear Reactor

Once ray-tracing calculations confirmed that the flux delivered by an existing nested Ni mirror design was detectable at the MIT Nuclear Reactor, two of the outer shells were built and tested. A photograph of the nested Ni mirrors is shown in Fig. 5.1. The mirrors have a system length of 3200 mm, a magnification of .25, and are defined by the geometric parameters listed in Table 1 of Appendix A. A 2 mm cadmium pinhole was placed 2,451 mm downstream from the 3×2 inch reactor window, at the first focus of the ellipsoid. A detector was placed at the focal spot, 3200 mm away from the cadmium pinhole. Ray tracing determined that only neutrons below 5 meV could be focused due to the low critical angle of Ni, experiment agreed with. However, there was discrepancy between the simulated HPD of .394 mm and the experimentally measured HPD of .7 mm. Most of the difference is attributed to slight distortions of the shells due to imperfect mechanical fitting of the holder.

Fig. 5.2 shows the detected image between the optics and the image focal plane for the two nested mirrors. The two light rings indicate that both mirrors contribute to the focal spot. Full data analysis and comparison with the calculations will be presented in a future publication.

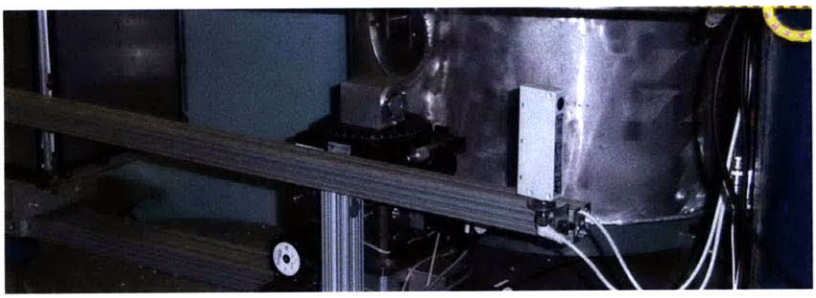

Figure 5-1: Experimental testing of nested Ni mirrors at the MIT Nuclear Reactor Laboratory.

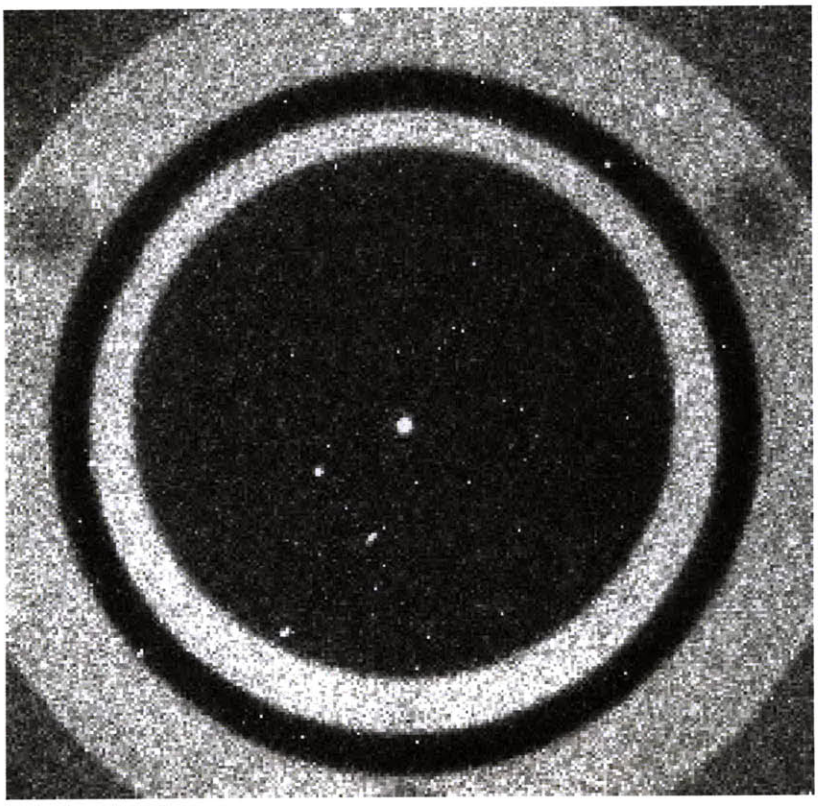

Figure 5-2: Two converging light rings from the two nested shells detected in front of the focal plane.

Chapter 6

Conclusions

Wolter optics is an existing x-ray optic that can be a viable focusing and imaging device for many neutron applications. The aim of this work was to investigate the effectiveness of Wolter Type I neutron microscope in focusing and imaging cold and thermal neutron sources by simulating the optics in a standard neutron ray-tracing software package.

To assess the focusing power of the optics, the simulation was used to optimize the mirrors for maximum flux density at the focal spot. Maximum flux density was found to occur for systems of lowest magnification (highest demagnification) and remained uniform and constant for varying source size. The maximum flux density delivered to the focal spot depended primarily on the cross-section of the mirrors, which was bounded by the critical angle of the mirrors, the size of the beam at the mirror entrance, and the physical length of the mirror segments. However, it was shown that it is possible to collect all the available flux by nesting the mirrors, which is particularly easy to do for Wolter geometry. The optimized system was compared to a scenario where no optics was present, demonstrating its high degree of focussing power.

To assess the imaging power of the optics, figure and finish errors for a real set of mirrors were simulated using geometry and Rayleigh-Rice perturbation theory respectively. The contribution of the surface errors to focal spot distortions were found to be small and could be partially credited to the fact that the optics requires

only two reflections.

Finally, the simulated set of nested Ni mirrors were built and tested at the MIT Nuclear Reactor Laboratory. The optics was shown to successfully concentrate neutron flux at the focal spot, where most experimental observations were in agreement with the simulation.

In conclusion, Wotler optics has the potential to be a useful addition to neutron beamline instrumentation, both for its ability to concentrate large beams onto small samples and for its near-perfect imaging capabilities. Through further investigation of Wolter optics, by both simulation and experiment, we can continue to assess the scope of these advantages and the extent of their effectiveness in different neutron applications.

Appendix A

Tables

Table A.1: Parameters of Ellipsoid and Hyperboloid in Nested Mirrors for Experiment

a_H [mm]	b_H [mm]	a_E [mm]	b_E [mm]	l_H [mm]	l_E [mm]	r_i [mm]	Θ_i [deg]
533.28210	7.2963186	2133.3819	14.592664	30.000	31.097	14.298	0.40000
533.28266	7.6654392	2133.3928	15.330969	30.000	31.097	15.021	0.42022
533.28237	8.0532169	2133.4040	16.106622	30.000	31.097	15.781	0.44148
533.28112	8.4605928	2133.4153	16.921513	30.000	31.096	16.579	0.46381

Bibliography

[1] K. S. Chon. Figure tolerance of a wolter type i mirror for a soft-x-ray microscope. *Applied Optics*, 46(14):2663+, May 2007.

[2] Th. Krist et al. *Neutron Supermirror Development*, chapter 22. Springer Berlin / Heidelberg, 2008.

[3] A. G. Michette. Rosat wide field camera mirrors. *Rep. Prog. Phys.*, 51:1525–1606, April 1988.

[4] Roger Pynn. Neutron scattering, a primer. *Los Alamos Science*, 1990.

[5] D. Spiga. Analytical evaluation of the x-ray scattering contribution to imaging degradation in grazing-incidence x-ray telescopes. *Astronomy and Astrophysics*, 468(2):775–784, June 2007.

[6] John C. Stover. *Optical Scattering: Measurement and Analysis.* Society of Photo-Optical Instrumentation Engineers, 1995.

[7] R. Willingale. Rosat wide field camera mirrors. *Applied Optics*, 27(8):1423–1429, April 1988.